# Mechanisms of Sum Frequency Generation from Liquid Benzene: Symmetry Breaking at Interface and Bulk Contribution

Tatsuya Kawaguchi, Kazuya Shiratori, Yuki Henmi, Tatsuya Ishiyama, and Akihiro Morita*

Department of Chemistry, Graduate School of Science, Tohoku University, Sendai 980-8578, Japan

ABSTRACT: Liquid benzene emits a significant sum frequency generation (SFG) signal of C−H stretching vibration, though it is composed of centrosymmetric molecules. The present paper theoretically elucidates the SFG spectrum from liquid benzene by considering two mechanisms, symmetry breaking at the interface and bulk contribution. Molecular dynamics and quantum chemical calculations reproduced the observed SFG spectrum and revealed that the two mechanisms are equally significant in the SFG spectrum of liquid benzene. At the interface, the SFG signal arises from local C−H stretching modes via the mixing of IR active and Raman active modes. The local modes are readily induced by the anisotropic environment at the interface. The observed SFG signal should also involve significant amount of quadrupole contribution, which is attributed to the IR active mode of the bulk liquid.
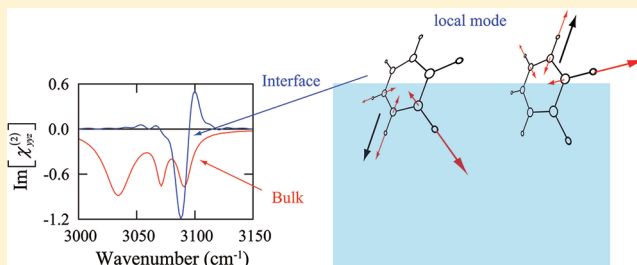
I. INTRODUCTION

Sum frequency generation (SFG) and second harmonic generation (SHG) are second-order nonlinear optical processes. Spectroscopies based on these phenomena have been widely utilized in surface science and related fields because of their sharp interface sensitivity.[1−3] The surface selectivity of the SFG and SHG originates from the selection rule that the induced dipole by the second-order susceptibility $\chi^{(2)}$ is forbidden in a medium with inversion symmetry. The SFG or SHG spectroscopy does not need vacuum in principle and thus is readily applicable to liquid interfaces which are not amenable to other surface probe techniques under vacuum conditions. In particular, the infrared-visible SFG spectroscopy is an excellent method to provide vibrational spectra of liquid interfaces such as gas−liquid, liquid−liquid, and solid−liquid interfaces.[4−8] The basic understandings of the SFG and SHG mechanisms are of great significance to clarify the microscopic nature of liquid interfaces.

The SFG or SHG spectroscopy as a surface probe is based on the symmetry breaking mechanism. At interfaces of ordinary liquids, the symmetry breaking gives rise to the SFG or SHG signal via anisotropic molecular orientation. Such preferential orientation at the interface is in contrast to the totally random orientation in the centrosymmetric bulk, where the contributions of molecular hyperpolarizabilities cancel with each other by their orientational average. However, when the molecules themselves have inversion symmetry such as benzene, the SFG and SHG may not be expected to occur from the interfaces even if these molecules are oriented at the interfaces. This is because each constituent molecule of inversion symmetry has null hyperpolarizability due to the rule of mutual exclusion. However, the SFG signal from liquid benzene was actually reported by Hommel and Allen.[9] This experimental result implies that the

above consideration for molecular orientation is not sufficient to account for the liquid benzene. In the present paper, we elucidate the SFG mechanism from the liquid benzene surface. While we have theoretically analyzed the SFG spectroscopy for the various liquid interfaces,[10−15] this paper is the first report on the theoretical SFG study on the liquid interface composed of centrosymmetric molecules.

There are two possibilities for explaining the observed SFG from liquid benzene. The first possibility is the symmetry breaking of the molecules themselves at the interface. Presumably, the symmetry of benzene molecule (D_{6h}) is broken at the interface, and thus the hyperpolarizability is induced there. If this is the case, the intermolecular interaction in the condensed phase is of primary importance for inducing the nonlinear susceptibility $\chi^{(2)}$ at the interface. The second possibility is the quadrupole contribution. It has been known that the quadrupole contribution to the SFG and SHG signals does not necessarily vanish in the centrosymmetric bulk for symmetry reasons.[16−19] The bulk quadrupolar contribution to the SFG of liquid benzene has been experimentally studied in the frequency range of visible and near-infrared.[20] On the theoretical side, there have been some pioneering works[21,22] on the bulk quadrupole contribution. Recently, we proposed a new theory on the quadrupole contribution to the SFG,[23] which allows us to quantitatively compare the electric dipole and quadrupole contributions in the observed SFG spectra.

In the present study, we examine the above two possible mechanisms for the SFG of liquid benzene using the molecular dynamics (MD) simulation and quantum chemical calculations.

To examine the first mechanism, accurate evaluation of $\chi^{(2)}$ at the interface is a key requisite which could incorporate the symmetry breaking of the molecules. We have developed computational methods of frequency-dependent $\chi^{(2)}$ at the interface by MD simulation,[24−26] and apply the methods to the liquid benzene surface in this study. The benzene molecule is represented using the charge response kernel (CRK) theory,[12,27−29] which have been successfully utilized to analyze the SFG spectra including water,[12] methanol,[14,15] and sulfuric acid.[13] The CRK theory can be easily extended to other molecules using ab initio or density functional theory calculations and used to develop a general molecular model suitable to the SFG calculations. To examine the second mechanism related to the quadrupole, we employed quantum chemical calculations of benzene properties. The calculated properties are utilized in the recent SFG theory on the quadrupole contribution[23,30] to estimate the bulk quadrupole contribution to the SFG. To our knowledge, this is the first study to calculate the interface and bulk contributions to the SFG in a comparable manner.

The remainder of this paper is organized as follows. In Section II, the molecular model of benzene is developed, and its performance is examined. Section III describes the MD simulation procedures and discusses bulk and surface properties of liquid benzene. Then the nonlinear susceptibility of the interface is computed and analyzed in Section IV. The bulk contribution of quadrupole origin is evaluated in Section V to clarify the comprehensive contributions to the SFG signal. The last section is devoted to the conclusion.

II. MOLECULAR MODEL

To calculate the SFG spectra by the time correlation formula,[25,26] a proper molecular model including molecular vibration and electronic polarization is needed. In the present model of benzene, the flexible properties are implemented by the internal potential, and the polarizable properties are described by the charge response kernel (CRK) theory.[27−29] In this section, we explain the flexible and polarizable model of benzene and examine the accuracy of the present model.

A. Force Field. The total potential energy of liquid benzene is described in the following form,

$$U = U_{\text{intra}} + U_{\text{C}} + U_{\text{LJ}} \tag{1}$$

where U_{intra} is the intramolecular potential, U_{C} is the Coulomb potential, and U_{LJ} is the Lennard−Jones potential. These terms are described below in order.

1. Intramolecular Potential. The intramolecular potential U_{intra} in eq 1 is the sum of the internal potential, u_{intra}, of each molecule. Therefore, we describe the expression of u_{intra} for a single benzene molecule.

As the internal coordinates of benzene, C−H bond distances ($r_1−r_6$), C−C distances ($R_1−R_6$), C−C−C angles ($\alpha_1−\alpha_6$), rolling angles ($\beta_1−\beta_6$), wagging angles ($w_1−w_6$), and C−C−C−C dihedral angles ($\tau_1−\tau_6$) are illustrated in Figure 1. These internal coordinates are obviously redundant, and we define $3N_{\text{atom}} − 6 = 30$ independent coordinates ($S_1−S_{30}$) using the internal coordinates as follows:

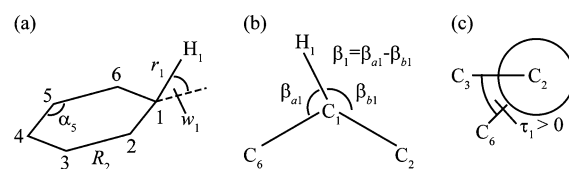$$A_{1g}: S_1 = \frac{1}{\sqrt{6}}(r_1 + r_2 + r_3 + r_4 + r_5 + r_6)$$

Figure 1. Illustrative definition of the internal coordinates of benzene. (a) Distances of C−H bonds, $r_1−r_6$, C−C bonds, $R_1−R_6$, C−C−C angles, $\alpha_1−\alpha_6$, and wagging angles, $w_1−w_6$. (b) Rolling angles, $\beta_1−\beta_6$. (c) Dihedral angles, $\tau_1−\tau_6$.

$$E_{2g}: S_2 = \frac{1}{2\sqrt{3}}(2r_1 - r_2 - r_3 + 2r_4 - r_5 - r_6)$$

$$E_{2g}: S_3 = \frac{1}{2}(r_2 - r_3 + r_5 - r_6)$$

$$B_{1u}: S_4 = \frac{1}{\sqrt{6}}(r_1 - r_2 + r_3 - r_4 + r_5 - r_6)$$

$$E_{1u}: S_5 = \frac{1}{2\sqrt{3}}(2r_1 + r_2 - r_3 - 2r_4 - r_5 + r_6)$$

$$E_{1u}: S_6 = \frac{1}{2}(r_2 + r_3 - r_5 - r_6)$$

$$A_{1g}: S_7 = \frac{1}{\sqrt{6}}(R_1 + R_2 + R_3 + R_4 + R_5 + R_6)$$

$$E_{2g}: S_8 = \frac{1}{2\sqrt{3}}(-R_1 + 2R_2 - R_3 - R_4 + 2R_5 - R_6)$$

$$E_{2g}: S_9 = \frac{1}{2}(-R_1 + R_3 - R_4 + R_6)$$

$$B_{2u}: S_{10} = \frac{1}{\sqrt{6}}(R_1 - R_2 + R_3 - R_4 + R_5 - R_6)$$

$$E_{1u}: S_{11} = \frac{1}{2}(R_1 - R_3 - R_4 + R_6)$$

$$E_{1u}: S_{12} = \frac{1}{2\sqrt{3}}(R_1 + 2R_2 + R_3 - R_4 - 2R_5 - R_6)$$

$$B_{2g}: S_{13} = \frac{1}{\sqrt{6}}(w_1 - w_2 + w_3 - w_4 + w_5 - w_6)$$

$$E_{1g}: S_{14} = \frac{1}{2\sqrt{3}}(2w_1 + w_2 - w_3 - 2w_4 - w_5 + w_6)$$

$$E_{1g}: S_{15} = \frac{1}{2}(w_2 + w_3 - w_5 - w_6)$$

$$A_{2u}: S_{16} = \frac{1}{\sqrt{6}}(w_1 + w_2 + w_3 + w_4 + w_5 + w_6)$$

$$E_{2u}: S_{17} = \frac{1}{2\sqrt{3}}(2w_1 - w_2 - w_3 + 2w_4 - w_5 - w_6)$$

$$E_{2u}: S_{18} = \frac{1}{2}(w_2 - w_3 + w_5 - w_6)$$

$$A_{2g}: S_{19} = \frac{1}{\sqrt{6}}(\beta_1 + \beta_2 + \beta_3 + \beta_4 + \beta_5 + \beta_6)$$

E_{2g}: $S_{20} = \dfrac{1}{2}(-\beta_2 + \beta_3 - \beta_5 + \beta_6)$

E_{2g}: $S_{21} = \dfrac{1}{2\sqrt{3}}(2\beta_1 - \beta_2 - \beta_3 + 2\beta_4 - \beta_5 - \beta_6)$

B_{2u}: $S_{22} = \dfrac{1}{\sqrt{6}}(\beta_1 - \beta_2 + \beta_3 - \beta_4 + \beta_5 - \beta_6)$

E_{1u}: $S_{23} = \dfrac{1}{2}(\beta_2 + \beta_3 - \beta_5 - \beta_6)$

E_{1u}: $S_{24} = \dfrac{1}{2\sqrt{3}}(-2\beta_1 - \beta_2 + \beta_3 + 2\beta_4 + \beta_5 - \beta_6)$

E_{2g}: $S_{25} = \dfrac{1}{2\sqrt{3}}(2\alpha_1 - \alpha_2 - \alpha_3 + 2\alpha_4 - \alpha_5 - \alpha_6)$

E_{2g}: $S_{26} = \dfrac{1}{2}(\alpha_2 - \alpha_3 + \alpha_5 - \alpha_6)$

B_{1u}: $S_{27} = \dfrac{1}{\sqrt{6}}(\alpha_1 - \alpha_2 + \alpha_3 - \alpha_4 + \alpha_5 - \alpha_6)$

B_{2g}: $S_{28} = \dfrac{1}{\sqrt{6}}(\tau_1 - \tau_2 + \tau_3 - \tau_4 + \tau_5 - \tau_6)$

E_{2u}: $S_{29} = \dfrac{1}{2}(\tau_1 - \tau_3 + \tau_4 - \tau_6)$

E_{2u}: $S_{30} = \dfrac{1}{2\sqrt{3}}(-\tau_1 + 2\tau_2 - \tau_3 - \tau_4 + 2\tau_5 - \tau_6)$

These coordinates, S_1-S_{30}, form bases of irreducible representations for molecular vibrations of benzene and are called natural internal coordinates. Using the natural internal coordinates, the internal potential of benzene molecule is represented in the following quadratic form,

$$u_{\text{intra}} = \frac{1}{2}\sum_{i=1}^{30}\sum_{j=1}^{30} k_{i,j}\Delta S_i \Delta S_j \tag{2}$$

where $k_{i,j}$ is a quadratic force constant and ΔS_i represents the displacement of S_i from the equilibrium values, that is, $\Delta S_i = S_i - S_i^{\text{eq}}$. The equilibrium values are determined from the experimental geometry,[31] $r_n^{\text{eq}} = 1.101$ Å, $R_n^{\text{eq}} = 1.399$ Å, $\alpha_n^{\text{eq}} = 120.0°$, and $\beta_n^{\text{eq}} = w_n^{\text{eq}} = \tau_n^{\text{eq}}$ $0.0°$.

In the potential of eq 2, the D_{6h} symmetry of benzene drastically reduces the independent number of the force constants $k_{i,j}$, since only the A_{1g} terms of the product $\Delta S_i \times \Delta S_j$ remain in eq 2. Consequently, the internal potential u_{intra} in eq 2 is represented in the following form including 34 independent nonzero constants,

$$u_{\text{intra}} = \frac{1}{2}\sum_{i=1}^{30} k_{i,i}\Delta S_i^2 + k_{1,7}\Delta S_1 \Delta S_7 + k_{13,28}\Delta S_{13}\Delta S_{28}$$
$$+ k_{4,27}\Delta S_4 \Delta S_{27} + k_{10,22}\Delta S_{10}\Delta S_{22}$$
$$+ k_{2,8}(\Delta S_2 \Delta S_8 + \Delta S_3 \Delta S_9)$$
$$+ k_{2,20}(\Delta S_2 \Delta S_{20} + \Delta S_3 \Delta S_{21})$$
$$+ k_{2,25}(\Delta S_2 \Delta S_{25} + \Delta S_3 \Delta S_{26})$$
$$+ k_{8,20}(\Delta S_8 \Delta S_{20} + \Delta S_9 \Delta S_{21})$$
$$+ k_{8,25}(\Delta S_8 \Delta S_{25} + \Delta S_9 \Delta S_{26})$$
$$+ k_{20,25}(\Delta S_{20} \Delta S_{25} + \Delta S_{21} \Delta S_{26})$$
$$+ k_{5,11}(\Delta S_5 \Delta S_{11} + \Delta S_6 \Delta S_{12})$$
$$+ k_{5,23}(\Delta S_5 \Delta S_{23} + \Delta S_6 \Delta S_{24})$$
$$+ k_{11,23}(\Delta S_{11} \Delta S_{23} + \Delta S_{12} \Delta S_{24})$$
$$+ k_{17,29}(\Delta S_{17} \Delta S_{29} + \Delta S_{18} \Delta S_{30}) \tag{3}$$

We note that a pair of diagonal elements $k_{i,i}$ for an E basis are equivalent, for example, $k_{2,2} = k_{3,3}$, $k_{4,4} = k_{5,5}$, and so forth. The quadratic force constants included in eq 3 are determined so as to be consistent to the experimental vibrational frequencies.[31] The detailed procedure to derive these values is given in Appendix A. The optimized results of $k_{i,j}$ are summarized in Table 1.

Table 1. Independent Force Constants (Atomic Units) for the Internal Potential of Benzene in Equation 3

i	j	$k_{i,j}$	i	j	$k_{i,j}$
1	1	0.3287	27	27	0.2927
2	2	0.3283	28	28	0.09155
4	4	0.3345	29	29	0.07690
5	5	0.3297	1	7	0.01180
7	7	0.4871	13	28	0.08935
8	8	0.4314	4	27	−0.03096
10	10	0.2610	10	22	−0.02187
11	11	0.4744	2	8	−0.006597
13	13	0.1456	2	20	0.002268
14	14	0.09387	2	25	−0.02009
16	16	0.06901	8	20	0.02845
17	17	0.1191	8	25	−0.05258
19	19	0.05725	20	25	−0.02264
20	20	0.06114	5	11	0.01395
22	22	0.05622	5	23	0.00001797
23	23	0.06337	11	23	0.01494
25	25	0.2861	17	29	0.06260

2. Coulomb Potential. The Coulomb potential is written as

$$U_{\text{C}} = \frac{1}{2}\sum_{i}^{\text{molecule}}\sum_{a=1}^{12} Q_{ai}V_{ai} - \frac{1}{2}\sum_{i}^{\text{molecule}}\sum_{a,b=1}^{12} K_{abi}V_{ai}V_{bi} \tag{4}$$

where Q_{ai} is the partial charge placed on site a of the molecule i, V_{ai} is the electrostatic potential at the site a of the molecule i, and K_{abi} is the CRK of the molecule i. The first term in eq 4 is ordinary Coulomb interaction energy, and the second term is the reorganization energy of polarization. The benzene molecule in the present model consists of 12 interaction sites located on six carbons and six hydrogens. These charges are determined via

electrostatic potential (ESP) fitting. The CRK, K_{ab}, is defined as the derivative of the ESP charge at the site a, Q_a, with respect to the electrostatic potential at the site b, V_b, $K_{ab} = \partial Q_a / \partial V_b$.[27]

The CRK allows for varying partial charge of the molecule i, Q_{ai}, by the electrostatic potential V_{bi} of the molecule i as follows,

$$Q_{ai} = Q_{ai}^{\,0} + \sum_{b=1}^{12} K_{abi} V_{bi} \tag{5}$$

and the electrostatic potential V_{bi} is determined by the Coulomb interactions from surrounding molecules j ($\neq i$),

$$V_{bi} = \sum_{j(\neq i)} \sum_{c=1}^{12} \frac{Q_{cj}}{r_{bi,cj}} f_{bi,cj} \tag{6}$$

where $r_{bi,cj}$ is the distance between the site b of the molecule i and the site c of the molecule j. $f_{bi,cj}$ is the damping function, which effectively remedies the shortcomings of the point charge interactions at a short range.[12] In the present study, the Gaussian type $f = f^{\text{Gauss}}$ is used with the width parameter $\xi = 0.65$ Å.[12]

In the present flexible model, the partial charges and CRK theory depend on the vibrational coordinates S. The conformational dependence is represented as

$$Q_a^{\,0} = Q_a^{\text{eq}} + \sum_{p=1}^{30} \left(\frac{\partial Q_a}{\partial S_p} \right)^{\text{eq}} \Delta S_p \tag{7}$$

$$K_{ab} = K_{ab}^{\text{eq}} + \sum_{p=1}^{30} \left(\frac{\partial K_{ab}}{\partial S_p} \right)^{\text{eq}} \Delta S_p \tag{8}$$

The equilibrium values Q_a^{eq}, K_{ab}^{eq}, $(\partial Q_a / \partial S_p)^{\text{eq}}$, and $(\partial K_{ab} / \partial S_p)^{\text{eq}}$ are determined by the quantum chemical calculations of B3LYP/cc-pVTZ with the GAMESS-UK package[32] modified by our group.[29] The calculated results of Q_a^{eq} and K_{ab}^{eq} are given in Tables 2 and 3, respectively. Their derivatives, $(\partial Q_a / \partial S_p)^{\text{eq}}$ and

Table 2. Site Charges in Equilibrium Geometry and Lennard–Jones Parameters for Benzene

	C	H
Q^{eq} (e)	−0.1087	0.1087
σ (Å)	3.55	2.30
ε (J/mol)	292.88	138.07

$(\partial K_{ab} / \partial S_p)^{\text{eq}}$, were derived by the five-point numerical differential for the calculated Q_a and K_{ab} with varying conformations.

3. Lennard–Jones Potential. The Lennard–Jones potential is expressed by

$$U_{\text{LJ}} = \sum_{i>j}^{\text{molecule}} \sum_{a,b=1}^{12} 4\varepsilon_{ab} \left\{ \left(\frac{\sigma_{ab}}{r_{ai,bj}} \right)^{12} - \left(\frac{\sigma_{ab}}{r_{ai,bj}} \right)^{6} \right\} \tag{9}$$

where σ_{ab} and ε_{ab} are the Lennard–Jones parameters, which were determined to reproduce the density, radial distribution functions, and vaporization enthalpy of liquid benzene, as discussed in Section III. The parameters for carbon and hydrogen atoms are tabulated in Table 2. The parameters between carbon and hydrogen were determined by the Lorentz–Berthelot rule: $\sigma_{\text{CH}} = (\sigma_{\text{C}} + \sigma_{\text{H}})/2$ and $\varepsilon_{\text{CH}} = (\varepsilon_{\text{C}} \varepsilon_{\text{H}})^{1/2}$.

B. Assessment of Model. The molecular model developed above is examined by investigating the polarizability of a single molecule and properties of benzene dimer. Other properties of

benzene in the condensed phase will be discussed in the next section.

1. Molecular Polarizability. In the CRK theory, the molecular polarizability tensor is derived from the CRK and the coordinates of the sites as

$$\alpha_{pq} = - \sum_{a,b=1}^{12} K_{ab} p_a q_b \tag{10}$$

where p_a and q_b are the Cartesian coordinates of the site a and b, respectively. The polarizability tensor thus derived for a benzene molecule in the equilibrium geometry is compared with the experimental value[31] in Table 4. The calculated in-plane components, α_{xx} and α_{yy}, are in good agreement with the experimental results, whereas the out-of-plane component α_{zz} is not represented by the present model. This is because the interaction sites are located on the molecular plane, and this shortcoming could be removed by adding some interaction sites out of the plane.[12] We have employed the present model though, since the present model properly describes the intermolecular interactions of dimer and liquid, as demonstrated below. In addition, the out-of-plane polarization is of secondary importance to elucidate the in-plane C–H stretching vibrations on which the present study focuses.

2. Properties of Benzene Dimer. The accuracy of the intermolecular interaction is evaluated through dimer properties. We calculated benzene dimer by the present CRK model in comparison with highly accurate ab initio calculations. The benzene dimer has three stable isomers, as illustrated in Figure 2, called parallel displaced (PD), sandwich, and T-shaped. Table 5 summarizes the structures and binding energies of the three isomers calculated by the present model and by QCISD(T)/aug-cc-pVTZ.[33] The present CRK model reproduces the results of the high accuracy calculations quite well, in a semiquantitative level.

III. MD SIMULATION

A. MD Conditions. In the present study, we simulated the bulk and the air–liquid interface of benzene. For the MD simulations of bulk liquid, $N = 256$ molecules were placed in a cubic cell of 33.56 Å in length with three-dimensional periodic boundary conditions. The cell dimension is consistent with the experimental density of liquid benzene, 0.8788 g/cm^3 at 20 °C.[31] For the MD simulations of the interface, $N = 256$ molecules were placed in a rectangular cell $L_x \times L_y \times L_z = 33.56$ Å $\times$ 33.56 Å $\times$ 167.78 Å with the three-dimensional periodic boundary conditions. The slab of liquid was formed inside the rectangular cell where the air–liquid interfaces were normal to the z-axis.

Both the simulations of bulk and interface were performed under the microcanonical (NVE) ensemble with an average temperature at 293.15 K. The equations of motion were integrated numerically by using the velocity Verlet algorithm with a time step of 0.544 fs. At each time step, the self-consistent eqs 5 and 6 for polarization were solved by iterations.[12] The long-range electrostatic forces were treated with the Ewald summation method, where the Ewald separation parameter was set to 0.187 Å^{-1}, and the real and reciprocal-space cutoffs were 16.78 Å and 1.17 Å^{-1}, respectively. These parameters are optimized to maximize computational performance.[34] The van der Waals interaction was calculated with a cutoff length of 16.78 Å.

We prepared 16 and 64 independent initial configurations for the bulk and the interface simulations, respectively. For both simulations, the molecules were initially placed at cubic lattice points in a cubic cell of 49.0 Å in length with a random orientation, and the initial velocities were randomly assigned

13172

dx.doi.org/10.1021/jp302684q | J. Phys. Chem. C 2012, 116, 13169–13182

Table 3. Charge Response Kernel (Atomic Units) of Benzene in Equilibrium Geometry

				K_{ab}^{eq}		
	$b = 1$	2	3	4	5	6
$a = 1$	−26.01					
2	16.65	−26.01				
3	−8.143	16.65	−26.01			
4	7.174	−8.143	16.65	−26.01		
5	−8.143	7.174	−8.143	16.65	−26.01	
6	16.65	−8.143	7.174	−8.143	16.65	−26.01
7	6.608	−2.706	0.8705	−1.114	0.8705	−2.706
8	−2.706	6.608	−2.706	0.8705	−1.114	0.8705
9	0.8705	−2.706	6.608	−2.706	0.8705	−1.114
10	−1.114	0.8705	−2.706	6.608	−2.706	0.8705
11	0.8705	−1.114	0.8705	−2.706	6.608	−2.706
12	−2.706	0.8705	−1.114	0.8705	−2.706	6.608
	$b = 7$	8	9	10	11	12
7	−3.444					
8	0.5799	−3.444				
9	0.06646	0.5799	−3.444			
10	0.3285	0.06646	0.5799	−3.444		
11	0.06646	0.3285	0.06646	0.5799	−3.444	
12	0.5799	0.06646	0.3285	0.06646	0.5799	−3.444

Table 4. Polarizability Tensor Components (10^{-25} cm^3) of Benzene in the Molecule-Fixed Coordinates

	CRK	exptl[31]
α_{xx}	123.6	123.1
α_{yy}	123.6	123.1
α_{zz}	0.0	63.5
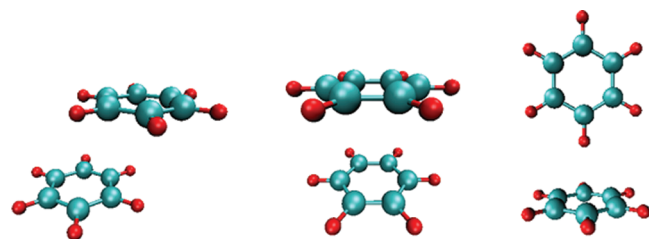
Figure 2. Three stable structures of benzene dimer: from left to right, parallel displaced (PD), sandwich, and T-shaped structures, respectively.

Table 5. Calculated Properties of Benzene Dimer by the Present CRK Model and QCISD(T)/aug-cc-pVTZ[33]^a

	center-of-mass distance (Å)		binding energy (kcal/mol)	
isomer	CRK	QCISD(T)	CRK	QCISD(T)
PD	3.510, 2.496	3.533, 1.715	2.276	2.550
sandwich	3.746	3.919	1.878	1.602
T-shaped	5.108	4.989	2.241	2.573

^{a}Three stable isomers are illustrated in Figure 2. For the parallel displaced (PD) isomer, horizontal and vertical displacements are shown.

according to the Maxwell−Boltzmann distribution at a temperature of 293.15 K. Then the cell length was gradually reduced to the target length, 33.56 Å, during time evolution for 16 ps. The system was subsequently equilibrated for 54 ps in the cubic cell of 33.56 Å to prepare the initial configurations for the bulk simulation. For the interface simulations, the cell was then elongated in the z direction to $L_z = 167.78$ Å, and further equilibration was performed for 108.8 ps. During the

equilibration run, the velocity scaling was carried out to hold the average temperature to 293.15 K. After the equilibrations, the bulk simulations were executed from 16 initial configurations in parallel for a total sampling time of 1.74 ns. The interface simulations were executed from 64 initial configurations in parallel for a total of 10.44 ns.

B. Bulk Properties. The MD simulation of liquid benzene demonstrated that the molecular model developed in Section II very well reproduces the properties of liquid benzene. We calculated the radial distribution functions, self-diffusion coefficient, and the enthalpy of vaporization by the MD simulation of the bulk liquid and the bulk density in the interior of the liquid slab. Figure 3 displays the calculated radial distribution functions in
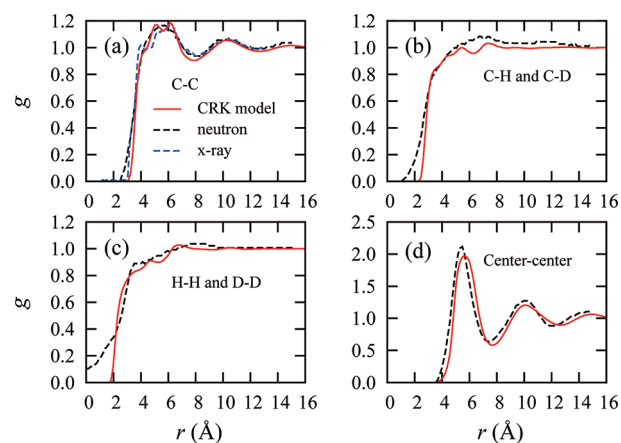

Figure 3. Site−site radial distribution functions of liquid benzene (a) C−C, (b) C−H, (c) H−H, and (d) center of mass-center of mass. Solid red lines represent the results of the CRK model. Dashed black and blue lines are the experimental results of neutron scattering[35] and X-ray diffraction,[36] respectively. For neutron scattering, C_6D_6 was used instead of C_6H_6.

comparison with experimental results of neutron scattering[35] and X-ray diffraction,[36] showing that the present MD calculation reproduces the experimental results well. In Table 6, the

Table 6. Properties for Bulk Liquid Benzene at 293.15 K

	CRK model	experiment
diffusion coefficient (10^{-9} m²/s)	2.04	2.21 ± 0.21^a
enthalpy of vaporization (kcal/mol)	8.300	8.148^b
density (g/cm³)	0.8784	0.8788^c

^{a}Reference 37 (298.15 K). ^{b}Reference 38. ^{c}Reference 31.

calculated self-diffusion coefficient, the enthalpy of vaporization, and the density of liquid benzene are compared with the experimental ones.[31,37,38] These calculated results indicate that the agreement with the experimental values is quite satisfactory.

C. Raman and Infrared Spectra. Next the vibrational Raman and infrared (IR) spectra for the liquid benzene in the C−H stretching frequency region are examined. A proper description of the C−H vibrations is important to discuss the vibrational SFG spectra in the next section. The benzene molecule has six vibrational modes of C−H stretching, as illustrated in Figure 4. Among the six modes, three modes (ν_2, ν_{7a}, ν_{7b}) are Raman active, while two other degenerate modes

v_{13}, F_1 v_{20a}, F_2 v_{20b}, F_3

v_2, F_4 v_{7a}, F_5 v_{7b}, F_6
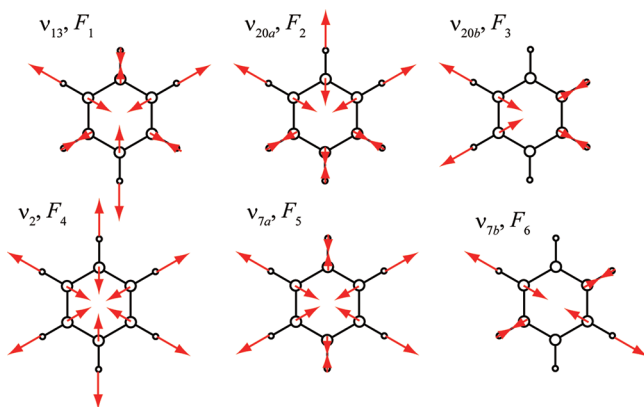
Figure 4. Six normal mode coordinates of the benzene C−H stretching vibrations, $F_1 - F_6$. Note that the ν_2 (F_4) and ν_7 (F_5, F_6) modes are Raman active, while ν_{20} (F_2, F_3) are IR active.

(ν_{20a}, ν_{20b}) are IR active. We calculated the Raman and IR spectra of the C−H vibrations by the MD simulation of the bulk liquid and compared the calculated lineshapes with the experimental ones.[9]

Raman Spectra. The lineshapes of the Raman spectra were calculated using the following equations,[10]

$$I_{\text{Raman}}^{\text{total}}(\omega) = I_{\text{Raman}}^{\text{pol}}(\omega) + \frac{2}{15}I_{\text{Raman}}^{\text{depol}}(\omega) \tag{11}$$

$$I_{\text{Raman}}^{\text{pol}}(\omega) = \frac{1}{2\pi}\int_{-\infty}^{\infty} dt\langle\overline{A}(t)\overline{A}(0)\rangle e^{-i\omega t} \tag{12}$$

$$I_{\text{Raman}}^{\text{depol}}(\omega) = \frac{1}{2\pi}\int_{-\infty}^{\infty} dt\langle\text{Tr}(B(t)B(0))\rangle e^{-i\omega t} \tag{13}$$

where $I_{\text{Raman}}^{\text{total}}(\omega)$, $I_{\text{Raman}}^{\text{pol}}(\omega)$, and $I_{\text{Raman}}^{\text{depol}}(\omega)$ are the line shape functions of total, polarized, and depolarized Raman spectra, respectively. $\overline{A} = (1/3)\text{Tr}A$ is the isotropic part of the polarizability of the entire system, and $B = A - \overline{A}I$ (I is the 3×3 unit matrix) is its anisotropic part. The left panels, a and c, of Figure 5 show the calculated and experimental[9] total Raman spectra, respectively. In the experimental spectrum the intense main band at 3063 cm⁻¹ is assigned to the ν_2 mode of A_{1g} symmetry, and the shoulder in the low frequency side at 3049 cm⁻¹ is to the ν_7 mode of E_{2g} symmetry.[39] The calculated Raman spectrum in panel a reproduces the experimental line shape of these bands well. One notices that a minor peak at 2950 cm⁻¹ in panel c is almost missing in the calculated spectrum of panel a. This peak is assigned to a bending overtone/combination band.[9]

Infrared Spectra. Figure 5b and d shows the calculated and experimental[9] IR spectra, respectively. The calculation was carried out using the following equation,[10]

$$I_{\text{IR}}(\omega) = \frac{1}{2\pi}\int_{-\infty}^{\infty} dt\langle\mathbf{M}(t)\mathbf{M}(0)\rangle e^{-i\omega t} \tag{14}$$

where $\mathbf{M}$ is the dipole moment of the entire system. Among the C−H stretching vibrations, the IR active modes are a set of degenerate (ν_{20a} and ν_{20b}) modes of E_{1u} symmetry at 3068 cm⁻¹.
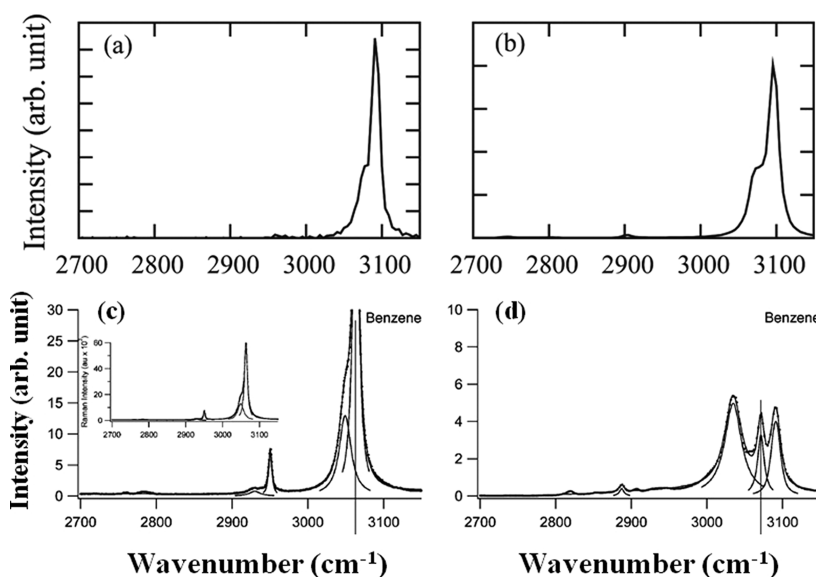

Figure 5. Raman spectra (a, c) and IR spectra (b, d) of liquid benzene by the present calculations (a, b) and experiment[9] (c, d). In panels c and d, deconvoluted peaks are shown by thin lines. The inset in c shows the full scale Raman spectrum. Reprinted with permission from ref 9. Copyright 2003, Royal Society of Chemistry.

In the experimental spectrum of panel d, however, this band is split into three peaks due to the Fermi resonance among ν_{20}, $\nu_8 + \nu_{19}$, and $\nu_1 + \nu_6 + \nu_{19}$.[40] The calculated IR spectrum of panel b does not reproduce the three split bands. This discrepancy is attributed to the fact that the present potential model does not incorporate the anharmonic coupling. We should be cautious of this point when we compare the calculated IR shape with the experimental one.

Nonetheless, it is interesting to notice that the calculated band in panel b shows a shoulder structure at about 3070 cm^{-1}. We attributed this shoulder to the Fermi resonance due to the kinetic coupling,[14,41] which is necessarily involved in the kinetic Hamiltonian of vibrations even though the potential function in eq 2 has no anharmonic coupling terms. To confirm the Fermi resonance, we conducted the empirical potential parameter shift analysis (EPSA).[15] We tentatively shifted the counterpart level from $\nu_8 + \nu_{19} = 3082$ cm^{-1} to 2742 cm^{-1}, by changing the relevant force constants $k_{20,20}$ ($= k_{21,21}$) = 0.0611 au and $k_{23,23}$ ($= k_{24,24}$) = 0.0634 au to 0.0211 and 0.0234, respectively, and thereby examined the effects on the calculated IR spectrum. This manipulation does not alter the fundamental frequencies of the C−H stretching vibrations, while it effectively removes coupling by the Fermi resonance, as illustrated in Figure 6b. Figure 6a
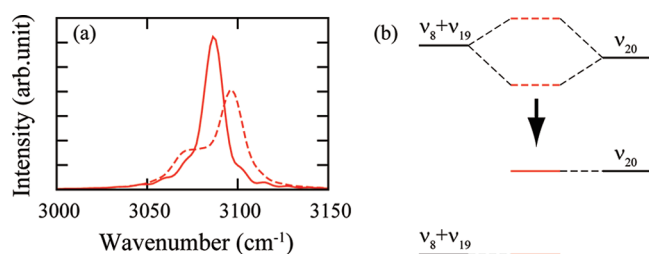
Figure 6. (a) Spectral change by the EPSA. The original IR spectrum (red dashed line) is compared with the IR spectrum calculated with the modified force constants (red solid line). (b) Diagram of the energy levels before and after the change. See the text.

shows the IR spectra in the C−H stretching region before and after the change of the force constants. By lifting the coupling we see that the shoulder disappears and that the two bands merge into a single peak in the middle of the original two bands. This behavior evidences mode mixing by the Fermi resonance.[15] Even though the force field includes no anharmonic coupling potential, the Fermi resonance could happen in the classical MD simulation.

It would be possible to incorporate anharmonic coupling into the intramolecular force field of eq 3 to improve the description of the Fermi resonance. In fact we have recently developed a modeling method of the Fermi resonance in the classical MD simulation[14,15] and successfully applied it to the methyl C−H stretching vibrations. Nevertheless the present model is useful enough to elucidate the mechanism of the SFG signal arising from benzene. The splitting of the observed bands is not essential for explaining the origin of the SFG, though it affects the line shape of SFG. We will take account of the splitting in an empirical manner in the interpretation of the SFG spectrum in Section V.

D. Orientation at Surface. We calculated the surface structure of liquid benzene by MD simulation of the liquid slab. Figure 7 shows the density and orientational profiles of the liquid slab along the surface normal. First we discuss the density profile shown in red. The calculated data of density (red circles) were
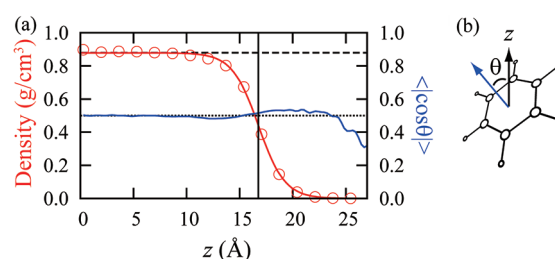

Figure 7. (a) Density and orientational profiles of liquid benzene along the surface normal coordinate z and (b) definition of orientational angle θ. For the density profile (red) in panel a, the red circles represent the calculated results, and the red solid line is the fitting curve by eq 15. The black horizontal dashed line corresponds to the experimental density (0.8788 g/cm^3) in the bulk liquid.[31] For the orientational profile (blue), the blue solid line represents the calculated results, and the black horizontal dotted line corresponds to 0.5, the value in random orientation. The vertical black solid line at z = 16.77 Å shows the position of the Gibbs dividing surface.

least-squares fitted as a function of the depth coordinate z using the following equation:[42−45]

$$\rho(z) = a[1 - \tanh\{b(|z| - c)\}] \tag{15}$$

where the origin of the z coordinate was set to the center of mass of the system. The optimized parameters in eq 15 are a = 0.4392 g/cm^3, b = 0.4039 Å^{-1}, c = 16.77 Å. The bulk density in the interior of the slab is $2a$ = 0.8784 g/cm^3, as shown in Table 6, which is in excellent agreement with the experimental density, 0.8788 g/cm^3.[31] The 10-90 thickness of the surface is estimated to be $1/(0.455b)$ = 5.44 Å. The position of Gibbs dividing surface is $z_{Gib} = c$ = 16.77 Å.

The molecular orientation at the surface is represented with the angle θ, illustrated in Figure 7b, between the surface normal and the normal vector to the benzene ring. Figure 7a shows the profile of average $|\cos\theta|$ with the blue line as a function of z. We found that $\langle |\cos\theta| \rangle$ is close to 0.5 in the interface as well as in the bulk region. In the interior of the bulk, $\langle |\cos\theta| \rangle \approx 0.5$ is consistent to the random orientation. To clarify the reason of 0.5 in the interface, we investigated the probability distribution of $|\cos\theta|$, $P(|\cos\theta|)$, in the bulk ($z < 10.6$ Å) and the interface (10.6 Å $< z <$ 20.1 Å) in Figure 8. This figure shows that the

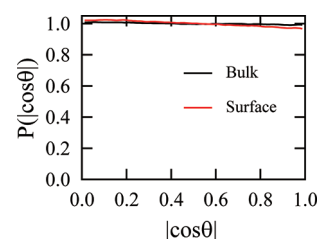**Figure 8.** Probability distributions of $|\cos\theta|$ in the bulk region ($z < 10.6$ Å, black line) and the surface (10.6 Å $< z <$ 20.1 Å, red line).

probability distribution is constant over $|\cos\theta|$ in the bulk, which is in accord with the random orientation. In the interface, the probability distribution is almost constant also. The above results indicate that the benzene molecules take nearly random orientation near the liquid−vapor interface as well as in the bulk liquid.

IV. SURFACE CONTRIBUTION

In this section, we investigate the nonlinear susceptibility $\chi^{(2)}$ of surface origin. As we discussed in Section I, the surface

contribution of $\chi^{(2)}$ must require that the inversion symmetry of benzene molecules is broken at the surface by intermolecular interactions. The intermolecular interactions of benzene can be properly described with the molecular model developed in Section II. We evaluate the amount and mechanism of symmetry breaking to induce the surface contribution of $\chi^{(2)}$ with the help of the MD simulation.

A. MD Calculation of $\chi^{(2)}$. The nonlinear susceptibility $\chi^{(2)}$ consists of the vibrational resonant term $\chi^{(2),res}$ and nonresonant term $\chi^{(2),nonres}$; $\chi^{(2)} = \chi^{(2),res} + \chi^{(2),nonres}$. The resonant term of the susceptibility can be calculated by the MD simulation using the time correlation function between the polarizability A and the dipole moment M of the entire system,[25,26]

$$\chi^{MD}_{pqr}(\omega_{IR}) = \frac{i\omega_{IR}}{k_BT} \int_0^\infty dt \langle A_{pq}(t)M_r(0)\rangle e^{i\omega_{IR}t} \quad (16)$$

where the suffixes p, q, and r stand for the space-fixed coordinates $x-z$. ω_{IR} is the IR frequency, k_B is the Boltzmann constant, T is the temperature, and the angular bracket $\langle\rangle$ denotes the statistical average. $A(t)$ and $M(t)$ in eq 16 are represented by the molecular model of benzene in Section II. On the other hand, the nonresonant term $\chi^{(2),nonres}$ is regarded to be a real constant over the IR frequency range in question.

To analyze the experimental SFG spectra, we have to consider polarization combination in the experimental SFG measurement, which is related to various pqr tensor component(s) of $\chi^{(2)}$. The previous experimental SFG study on the air/benzene interface[9] employed the SSP combination, where the sum frequency, visible, and infrared lights are S-, S-, and P-polarized, respectively. The observed intensity spectrum of the SSP-polarized SFG is expressed using the square of the yyz component; $I_{SSP} \propto |\chi^{(2)}_{yyz}|^2$. In the following, we focus on the SSP combination and mainly deal with $\chi^{(2)}_{yyz}$, in particular its imaginary part $Im[\chi^{(2)}_{yyz}]$. $Im[\chi^{(2)}_{yyz}]$ is more informative than $|\chi^{(2)}_{yyz}|^2$ obtained by the usual intensity spectrum, since the former contains the phase information of $\chi^{(2)}$ in addition to its amplitude. In particular, the sign of $Im[\chi^{(2)}_{yyz}]$ reflects the orientation of the transition dipole moment,[24] as discussed below. The imaginary part of $\chi^{(2)}_{yyz}$ is equivalent to that of the resonant term $\chi^{(2),res}$ and hence χ^{MD}_{yyz} ($Im[\chi^{(2)}_{yyz}] = Im[\chi^{MD}_{yyz}]$), since the nonresonant term $\chi^{(2),nonres}$ is real. The MD calculation can directly derive $Im[\chi^{(2)}]$ by eq 16, whereas $Im[\chi^{(2)}]$ is not amenable to the conventional SFG experiment except for the recent phase-sensitive SFG measurement.[6,46–48]

B. Calculated Results of $Im[\chi^{(2)}]$. The black solid line in Figure 9 shows the calculated $Im[\chi^{(2)}_{yyz}]$ for the air–liquid interface of benzene. The spectrum of $Im[\chi^{(2)}_{yyz}]$ shows a main negative peak at about 3080 cm^{-1} and a positive peak at 3100 cm^{-1}. These bands imply the symmetry breaking at the interfacial region, and the sign of these bands reflects the transition moments of the relevant vibrations. Details of these mechanism are discussed in the next subsection IV, C.

We then analyze the depth profile of $Im[\chi^{(2)}_{yyz}]$ to identify the depth from which the sum frequency output generates. The formula of $\chi^{(2)}$ in eq 16 includes the polarizability A and the dipole moment M of the entire system, which are formally represented as the sum of those of the constituent molecules,

$$A_{pq} = \sum_i^{molecules} \alpha_{pq,i} \qquad M_r = \sum_j^{molecules} \mu_{r,j} \quad (17)$$

where $\alpha_{pq,i}$ denotes the polarizability component of the molecule i, and $\mu_{r,j}$ the dipole component of the molecule j. Note that $\alpha_{pq,i}$
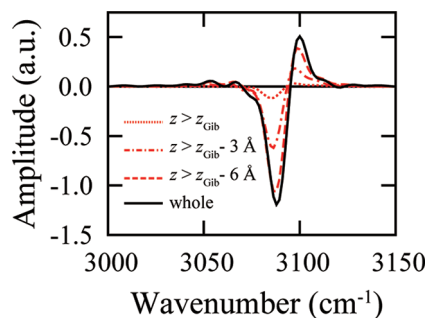

Figure 9. Convergence behavior of $Im[\chi^{(2)}_{yyz}]$ with an expanding surface region. See the discussion in Section IV, B.

and $\mu_{r,j}$ include the local field correction and the induced polarization.[12] In the summation of eq 17, we could restrict the molecules within the range of $z > z_{thres}$, and accordingly calculate $\chi^{(2)}$ by eq 16 in the restricted region. By gradually expanding the region (lowering the threshold z_{thres}), we can see the convergence behavior of $\chi^{(2)}$. Figure 9 show the results of $Im[\chi^{(2)}_{yyz}]$ by setting $z_{thres} = z_{Gib}, z_{Gib} - 3$ Å, and $z_{Gib} - 6$ Å. (Note that $z_{Gib} = 16.77$ Å in the density profile of Figure 7.) We found that the result with $z_{thres} = z_{Gib} - 6$ Å shows nearly a converged amplitude, indicating that the surface SFG signals mostly come from the shallow region of $z > z_{Gib} - 6$ Å. We also found that both the positive and negative peaks originate from the region in the same depth.

Equation 17 allows us to decompose the resonant part of $\chi^{(2)}$ into self part and cross part in the following form,

$$\chi^{MD}_{pqr}(\omega_{IR}) = \frac{i\omega_{IR}}{k_BT} \int_0^\infty dt \sum_{i,j}^{molecules} \langle \alpha_{pq,i}(t)\mu_{r,j}(0)\rangle e^{i\omega_{IR}t}$$

$$= \frac{i\omega_{IR}}{k_BT} \int_0^\infty dt \sum_i \langle \alpha_{pq,i}(t)\mu_{r,i}(0)\rangle e^{i\omega_{IR}t}$$

$$+ \frac{i\omega_{IR}}{k_BT} \int_0^\infty dt \sum_{i\neq j} \langle \alpha_{pq,i}(t)\mu_{r,j}(0)\rangle e^{i\omega_{IR}t}$$

$$= \chi^{MD,self}_{pqr}(\omega_{IR}) + \chi^{MD,cross}_{pqr}(\omega_{IR}) \quad (18)$$

Figure 10 shows the comparison of $Im[\chi^{(2)}_{yyz}] = Im[\chi^{MD,self}_{yyz} + \chi^{MD,cross}_{yyz}]$ (red line) with $Im[\chi^{MD,self}_{yyz}]$ (blue line). The

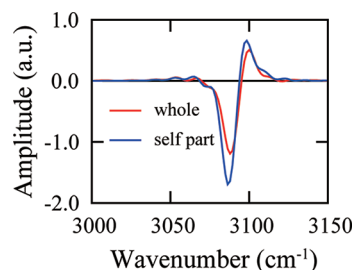**Figure 10.** Comparison of the whole amplitude of $Im[\chi^{(2)}_{yyz}]$ (red line) with that of the self part $Im[\chi^{MD,self}_{yyz}]$ (blue line) in eq 18.

difference between the two lines is attributed to the cross part. We find from this figure that the self part dominates the whole amplitude of $Im[\chi^{(2)}_{yyz}]$, while the cross part has a minor contribution. Therefore, we will mainly analyze the self part to qualitatively assign the vibrational modes in the remainder of this section.

C. Assignment of Vibrational Mode. Next, we assign the vibrational modes for the calculated bands of $Im[\chi^{(2)}_{yyz}]$ in

Figure 9. The vibrational bands in the frequency range of 3000–3150 cm^{-1} should be attributed to the C−H stretching modes and related combination modes. We decompose the second-order susceptibility into the relevant normal modes as follows.

The molecular polarizability and dipole moment are expanded by the normal mode coordinate F_m,

$$\alpha_{yy,i}(\{F\}, t) = \alpha_{yy}(\{F^{eq}\}) + \sum_m^{vib} \left(\frac{\partial \alpha_{yy}}{\partial F_m}\right)^{eq} \Delta F_{m,i}(t) + \cdots \tag{19}$$

$$\mu_{z,i}(\{F\}, t) = \mu_z(\{F^{eq}\}) + \sum_m^{vib} \left(\frac{\partial \mu_z}{\partial F_m}\right)^{eq} \Delta F_{m,i}(t) + \cdots \tag{20}$$

The normal mode coordinates F_m are derived from the Hessian matrix in Appendix A, and the six C−H stretching modes F_1−F_6 are illustrated in Figure 4. The displacements of these normal mode coordinates ΔF_1−ΔF_6 can be represented with a linear combination of those of the natural internal coordinates ΔS_1−ΔS_{30} given in Section II. Equations 19 and 20 indicate that the vibrational components of $\alpha(t)$ and $\mu(t)$ are driven by the vibrations of the normal mode coordinates $F_m(t)$. By substituting these equations into the self part of eq 18, we obtain an approximate form,

$$\chi_{yyz}^{MD,self} \approx \sum_i^{molecule} \sum_{m,n}^{CHstr} \frac{i\omega_{IR}}{k_B T} \left(\frac{\partial \alpha_{yy}}{\partial F_m}\right)^{eq} \left(\frac{\partial \mu_z}{\partial F_n}\right)^{eq}$$

$$\times \int_0^\infty dt \langle \Delta F_{m,i}(t) \Delta F_{n,i}(0) \rangle e^{i\omega_{IR}t}$$

$$= \sum_{m,n}^{CHstr} \rho_{mn}(\omega_{IR}) \tag{21}$$

where $(\partial \alpha_{yy}/\partial F_m)^{eq}$ and $(\partial \mu_z/\partial F_n)^{eq}$ are regarded as constant during the C−H vibrational motion. Equation 21 takes account of six C−H stretching modes, F_1−F_6, for the qualitative assignment of the C−H vibrations, since contributions from other modes are quite minor in the frequency range of this study. $\rho_{mn}(\omega_{IR})$ in eq 21 is defined as follows,

$$\rho_{mn}(\omega_{IR}) = \frac{i\omega_{IR}}{k_B T} \sum_i^{molecule} \left(\frac{\partial \alpha_{yy}}{\partial F_m}\right)^{eq} \left(\frac{\partial \mu_z}{\partial F_n}\right)^{eq}$$

$$\int_0^{Tseg} dt \langle \Delta F_{m,i}(t) \Delta F_{n,i}(0) \rangle e^{i\omega_{IR}t} \tag{22}$$

which represents the contribution of the correlation between normal modes m and n to the second-order susceptibility.

ρ_{mn} in eq 22 is evaluated in the following manner. The time correlation function, $\langle \Delta F_{m,i}(t) \Delta F_{n,i}(0) \rangle$, is calculated with the MD simulation of the benzene surface. During the MD trajectories, the time correlation function for each molecule i is stored in each time segment of $T_{seg} = 1.11$ ps. This time interval is chosen so as to be shorter than the rotational relaxation time of benzene evaluated by the MD simulation, that is, 2.30 ps for in-plane rotation and 3.11 ps for out-of-plane. Therefore, the molecular orientation is nearly invariant within this time segment. The prefactor in eq 22, $(\partial \alpha_{yy}/\partial F_m)^{eq}(\partial \mu_z/\partial F_n)^{eq}$, is determined for each molecule i and each time segment, on the basis of the instantaneous molecular orientation. The prefactor was calculated using the present CRK model for an isolated benzene molecule. The time correlation function multiplied with

the prefactor is averaged over all of the molecules and time segments to derive $\rho_{mn}(\omega_{IR})$ in eq 22.

The purpose of calculating ρ_{mn} in eq 22 is to qualitatively clarify the vibrational modes in the SFG spectrum. We note that the assignment of the normal modes is given with a pair of (m, n). Only the off-diagonal elements of ρ_{mn} $(m \neq n)$ remain since the prefactor of the diagonal elements $(m = n)$ should vanish in eq 22, due to the mutual exclusion rule of infrared and Raman. Figure 11a displays the main elements of $\rho_{mn}(\omega_{IR})$ as a function
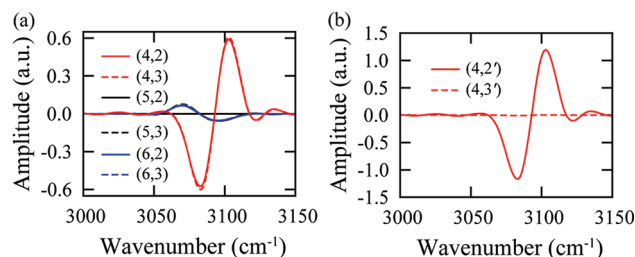
Figure 11. Panel a: main (m, n) elements of ρ_{mn} in eqs 21 and 22. The degenerated $(4, 2)$ and $(4, 3)$ elements are transformed to $(4, 2')$ and $(4, 3')$ in the space-fixed coordinates, displayed in panel b.

of the frequency ω_{IR}, indicating that the $(4, 2)$ and $(4, 3)$ elements have dominant contributions. The mode 4 (ν_2) is a Raman active A_{1g} mode, while the modes 2 and 3 (ν_{20}) are IR active E_{1u} modes, as illustrated in Figure 4. The correlation between the different symmetry implies a mechanism of symmetry breaking at the interface.

The symmetry breaking at the surface becomes more obvious by properly choosing the bases of the IR active E_{1u} modes, F_2 and F_3. The transition dipoles of the E_{1u} modes are located in the molecular plane, and the transition dipole vectors corresponding to F_2 and F_3 are defined as $\mathbf{e}_a$ and $\mathbf{e}_b$, respectively. Since the bases of the degenerate modes F_2 and F_3 are not unique, they could be unitarily transformed to F_2' and F_3' in the space-fixed coordinates, and accordingly the transition dipoles change to $\mathbf{e}_a'$ and $\mathbf{e}_b'$. For a given molecular orientation at the surface illustrated in Figure 12a, we define two orthogonal transition dipoles $\mathbf{e}_a'$ and $\mathbf{e}_b'$
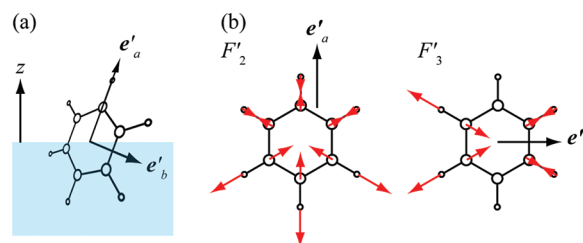
Figure 12. (a) Transition dipole vectors $\mathbf{e}_a'$ and $\mathbf{e}_b'$ in the space-fixed coordinate. (b) The transformed normal mode coordinates F_2' and F_3' in relation to their transition dipole $\mathbf{e}_a'$ and $\mathbf{e}_b'$.

so that $\mathbf{e}_b'$ is perpendicular to the space-fixed z-axis and $\mathbf{e}_a'$ is perpendicular to $\mathbf{e}_b'$. The new normal mode coordinates F_2' and F_3' are defined so as to satisfy

$$F_2 \mathbf{e}_a + F_3 \mathbf{e}_b = F_2' \mathbf{e}_a' + F_3' \mathbf{e}_b' \tag{23}$$

and thus

$$\begin{pmatrix} F_2' \\ F_3' \end{pmatrix} = \begin{pmatrix} (\mathbf{e}_a' \cdot \mathbf{e}_a) & (\mathbf{e}_a' \cdot \mathbf{e}_b) \\ (\mathbf{e}_b' \cdot \mathbf{e}_a) & (\mathbf{e}_b' \cdot \mathbf{e}_b) \end{pmatrix} \begin{pmatrix} F_2 \\ F_3 \end{pmatrix} \tag{24}$$

Using the coordinates $F_2{'}$ and $F_3{'}$ instead of F_2 and F_3, we performed the calculations of ρ_{mn} in eq 22, and the results are shown in the panel b of Figure 11. We clearly see that the correlation between F_4 and $F_2{'}$ is dominant while the correlation between F_4 and $F_3{'}$ is negligible. The correlation between the F_4 and $F_2{'}$ vibrations implies that these vibrational motions with different symmetries have some coherence, indicating that the modes 4 and 2′ are mixed to form a local mode at the interface.

We further elucidate the phase of the (4, 2′) element in Figure 11b. In the (4, 2′) element of eq 22, we note that the prefactor $(\partial\alpha_{yy}/\partial F_4)^{eq}(\partial\mu_z/\partial F_2{'})^{eq}$ is positive in the space-fixed coordinates, since $(\partial\alpha_{yy}/\partial F_4)^{eq} < 0$ and $(\partial\mu_z/\partial F_2{'})^{eq} < 0$. In the totally symmetric C−H stretching mode ν_2 (F_4), the stretching of the C−H bonds decreases the isotropic polarizability. This is understood because the C−H stretching shrinks the C_6 skeleton ring of benzenes. Figure 13 depicts the phase relation of $\rho_{42'}$ and
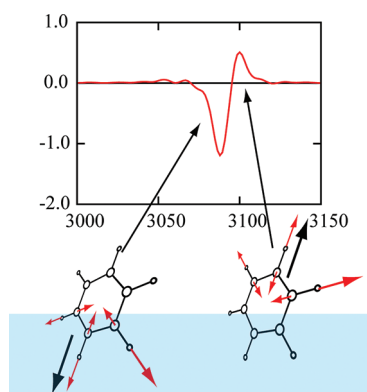

Figure 13. Assignment for the two bands with local modes.

the mode mixing. The positive phase of $\rho_{42'}$ at about 3100 cm^{-1} corresponds to in-phase mixing of the modes F_4 and $F_2{'}$, which results in a local mode that the C−H bonds pointing upward vibrate more vigorously than those downward. On the other hand, the negative phase of $\rho_{42'}$ at about 3080 cm^{-1} corresponds to the out-of-phase mixing of the modes F_4 and $F_2{'}$, generating a local mode that the C−H bonds pointing downward vibrate mainly. In summary, the mixing of the normal modes F_4 (ν_2) and $F_2{'}$ (ν_{20}) generate two local modes at the surface with opposite signs, as depicted in Figure 13, which slightly split in the frequency due to the different environment of the liquid side and the gas side. We further notice in Figure 10 that the negative amplitude of $\mathrm{Im}[\chi^{(2)}_{yyz}]$ is more emphasized than the positive one, whereas $\rho_{42'}$ in Figure 11 shows a nearly equivalent amount of positive and negative amplitudes. This difference in the amplitude in Figure 10 is attributed to the solvent effect that the transition dipole $(\partial\mu_z/\partial F_2{'})$ is enhanced in the liquid environment more than in the gas phase. Such perturbation is not incorporated in the qualitative estimate of ρ_{mn} in eq 22, as the prefactor $(\partial\alpha_{yy}/\partial F_4)^{eq}(\partial\mu_z/\partial F_2{'})^{eq}$ in eq 22 is estimated for an isolated benzene molecule.

Finally we feature the mechanism of the symmetry breaking discussed above. The six normal modes of the C−H stretching vibrations of benzene are in close energy levels. Those quasi-degenerate normal modes could easily interact with each other in terms of their energetics, whereas their molecular symmetry prevents interaction between modes of different symmetry. In such situation, even a weak perturbation to break the symmetry could readily mix these vibrational states. Molecules at the interface feel anisotropic perturbation, which causes the mode

mixing between the IR active mode ν_{20} (F_2, F_3) and the Raman active mode ν_2 (F_4) to form the local modes.

V. BULK CONTRIBUTION

As discussed in Section I, the SFG of quadrupole origin is allowed under the inversion symmetry, and thus quadrupolar signals of SFG may take place in centrosymmetric bulk media. Such quadrupolar contributions might be substantial in the liquid benzene consisting of centrosymmetric molecules. In this section, we evaluate the quadrupole contribution in the SFG signal of benzene and thereby present a comprehensive analysis of the benzene SFG.

A. Theory. First we briefly summarize the SFG theory on the quadrupole contributions[23] which the following computation is based upon. In the conventional SFG theory based on the dipole approximation, the intensity of SSP-polarized SFG is expressed using the yyz component of the second-order nonlinear susceptibility $\chi^{(2)}$,

$$I_{SSP} \propto |\chi^{(2)}_{yyz}|^2 \tag{25}$$

When we take the quadrupole contributions into account, $\chi^{(2)}$ in eq 25 should be replaced with an extended susceptibility $\chi^{(2)}_q$ incorporating the quadrupole effects,[23]

$$\chi^{(2)}_q = \chi^{ID} + \chi^{IQ} + \chi^{IQB} + \chi^{B} \tag{26}$$

where χ^{ID} originates from the induced dipole and χ^{IQ}, χ^{IQB}, and χ^{B} from the induced quadrupole. Among the three terms of quadrupole origin, χ^{IQ} represents the induced dipole by the electric field gradient at the surface and thus is considered to be a part of the surface dipole. The MD calculation by eq 16 incorporates this contribution in principle in the induced dipole of the surface, since the molecular model can describe the dielectric response to the local field and its gradient. The remaining two terms, χ^{IQB} and χ^{B}, reflect properties of the bulk medium and are not considered in the MD calculation of the surface system. Therefore, we calculate these bulk contributions of liquid benzene and compare them with the surface contributions in the SFG spectrum.

The χ^{IQB} term is expressed by the quadrupole susceptibility χ^{Q} and local field correction factor[49] s of the bulk liquid as follows,[23]

$$\chi^{IQB}_{pqr}(\omega_{SF}, \omega_{vis}, \omega_{IR})$$
$$= \chi^{Q}_{pqrz}(\omega_{SF}, \omega_{vis}, \omega_{IR})s_p(\omega_{SF})s_q(\omega_{vis})s_r(\omega_{IR}) \tag{27}$$

where ω_{SF}, ω_{vis}, and ω_{IR} denote the frequencies of SFG, visible, and IR, respectively. Since we consider the electronically off-resonant conditions, the ω_{IR} dependence of χ^{IQB} and χ^{Q} is of primary importance in relation to the experiment. χ^{Q}_{pqrs} is the quadrupole susceptibility, that is,

$$Q_{pq}(\omega_{SF}) = \chi^{Q}_{pqrs}(\omega_{SF}, \omega_{vis}, \omega_{IR})E_r(\omega_{vis})E_s(\omega_{IR}) + \cdots \tag{28}$$

which relates the induced quadrupole $Q_{pq}(\omega_{SF})$ in a unit volume of the bulk liquid to the electric fields $E_r(\omega_{vis})$ and $E_s(\omega_{IR})$. Note that χ^{Q}_{pqrs} is a fourth-rank tensor, and accordingly it does not vanish in a centrosymmetric medium. In isotropic media, fourth-rank tensors χ_{pqrs} in general have only the following nonvanishing elements,

13178

dx.doi.org/10.1021/jp302684q | J. Phys. Chem. C 2012, 116, 13169−13182

$$\chi_{pqpq} \equiv \chi_1 \qquad \chi_{ppqq} \equiv \chi_2 \qquad \chi_{pqqp} \equiv \chi_3$$
$$(p \neq q)$$
$$\chi_{pppp} = \chi_1 + \chi_2 + \chi_3 \qquad (29)$$

The relations of eq 29 greatly simplify the expressions of the fourth-rank tensor properties of the isotropic bulk.

The bulk term χ^B varies with the experimental geometry of SFG measurement, such as the incident angles and direction of signal detection. In the experimental geometry depicted in Figure 14, the χ^B term for the SSP polarization is represented in the following form,[23]
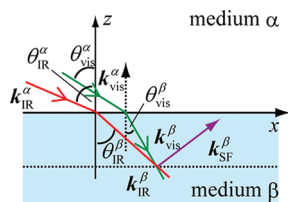
Figure 14. Geometry of experimental SFG measurement.

$$\chi^B_{yyz}(\omega_{SF}, \omega_{vis}, \omega_{IR})$$

$$= l_C \zeta_2^{Q1}(\omega_{SF}, \omega_{vis}, \omega_{IR}) \frac{(\mathbf{k}^\beta_{vis} \times \mathbf{k}^\beta_{IR})_y}{\mathbf{k}^\beta_{IR,x}} s_y(\omega_{SF}) s_y(\omega_{vis}) s_z(\omega_{IR})$$

$$(30)$$

where $\mathbf{k}^\beta_{SF}$, $\mathbf{k}^\beta_{vis}$, and $\mathbf{k}^\beta_{IR}$ are the wave vectors in the medium β (liquid benzene) for the sum frequency, visible, and infrared beams, respectively. l_c denotes the coherence length defined by

$$l_C \equiv \frac{1}{k^\beta_{vis,z} + k^\beta_{IR,z} - k^\beta_{SF,z}} \qquad (31)$$

In the scheme of detecting reflected SFG signals, $k^\beta_{SF,z}$ has the opposite sign to $k^\beta_{vis,z} + k^\beta_{IR,z}$.

$\zeta_2^{Q1}(\omega_{SF}, \omega_{vis}, \omega_{IR})$ is defined in the following,

$$\zeta_2^{Q1}(\omega_{SF}, \omega_{vis}, \omega_{IR})$$
$$\equiv \chi_2^{D1}(\omega_{SF}, \omega_{vis}, \omega_{IR}) - \chi_2^Q(\omega_{SF}, \omega_{vis}, \omega_{IR}) \qquad (32)$$

where χ^{D1} is a kind of second-order susceptibility in response to the gradient of visible electric field $\nabla E(\omega_{vis})$ and the IR field $E(\omega_{IR})$.[23] Since both χ^{D1} and χ^Q in eq 32 are fourth-rank tensors, their ppqq components in the isotropic bulk liquid are denoted with the subscript 2 after eq 29.

B. Computational Procedure. To evaluate the bulk contributions, χ^{IQB} and χ^B, the following properties are needed: (i) χ^{D1} and χ^Q; (ii) the local field correction s, and (iii) the experimental geometry. We explain the procedures for evaluating these properties as follows.

i. χ^{D1} and χ^Q. These susceptibilities for the bulk liquid are modeled by calculating the corresponding quadrupolar hyperpolarizabilities of a benzene molecule. Using the energy representation of the hyperpolarizabilities and the harmonic approximation, the vibrationally resonant components of the corresponding quadrupolar hyperpolarizabilities, $X^{D1,res}$ and $X^{Q,res}$, are represented in the following forms,[24,30]

$$X^{D1,res}_{pqrs}(\omega_{IR}) \approx - \sum_m^{CHstr} \frac{1}{2\omega_m} \frac{1}{\omega_{IR} - \omega_m + i\gamma_m} \left(\frac{\partial \beta'_{pqs}}{\partial F_m}\right)^{eq} \left(\frac{\partial \mu_r}{\partial F_m}\right)^{eq}$$

$$(33)$$

$$X^{Q,res}_{pqrs}(\omega_{IR}) \approx - \sum_m^{CHstr} \frac{1}{2\omega_m} \frac{1}{\omega_{IR} - \omega_m + i\gamma_m} \left(\frac{\partial \beta_{pqr}}{\partial F_m}\right)^{eq} \left(\frac{\partial \mu_s}{\partial F_m}\right)^{eq}$$

$$(34)$$

where μ is the dipole moment of the benzene molecule. β and β' are the quadrupole polarizability of the molecule defined in ref 30. ω_m and γ_m are the resonant frequency and the width for the normal mode m. The coordinate of the normal mode F_m is given so that its reduced mass is unity. In the summation over the mode m in eqs 33 and 34, we consider the C−H stretching vibrational modes in the frequency range of this study.

The derivative quantities in eqs 33 and 34, $(\partial \beta'/\partial F)^{eq}$, $(\partial \beta/\partial F)^{eq}$, and $(\partial \mu/\partial F)^{eq}$, were calculated for a benzene molecule in the liquid phase in molecule-fixed coordinates. The quantum chemical calculations were performed at the level of B3LYP/cc-pVTZ using Gaussian 03,[50] where the solvent effect of benzene was taken into account by the PCM model[51] with the dielectric constant of 2.247. The derivative with respect to the normal mode coordinate m was carried out by the 5-point numerical differential. The products of the calculated derivatives, $(\partial \beta'_{pqs}/\partial F_m)^{eq} \cdot (\partial \mu_r/\partial F_m)^{eq}$ and $(\partial \beta_{pqr}/\partial F_m)^{eq} \cdot (\partial \mu_s/\partial F_m)^{eq}$, were further averaged over isotropic orientation to obtain the nonvanishing elements in eq 29.

In eqs 33 and 34, we notice from the selection rule that only the IR-active mode ν_{20} contributes to $X^{D1,res}$ and $X^{Q,res}$. The ν_{20} mode manifests three split bands in the experimental IR spectrum in Figure 5d, due to the Fermi resonance mentioned before. The relative intensity of the three bands reflects the weight factor of the bright ν_{20} component in the three split eigenstates. Since the same eigenstates observed in the IR spectrum of bulk liquid are manifested in $X^{D1,res}$ and $X^{Q,res}$ also, we employ the experimental IR line shape of the ν_{20} mode for representing the spectra of $X^{D1,res}$ and $X^{Q,res}$. Suppose the experimental IR line shape in Figure 5d is represented with three Lorentz functions in the 3000−3150 cm^{-1} range,

$$I_{IR}(\omega_{IR}) \propto -\text{Im}\left[\frac{C^{(1)}}{\omega_{IR} - \omega^{(1)} + i\gamma^{(1)}} \right.$$

$$\left. + \frac{C^{(2)}}{\omega_{IR} - \omega^{(2)} + i\gamma^{(2)}} + \frac{C^{(3)}}{\omega_{IR} - \omega^{(3)} + i\gamma^{(3)}} \right]$$

$$= -\text{Im}[g(\omega_{IR})] \qquad (C^{(1)} + C^{(2)} + C^{(3)} = 1) \qquad (35)$$

The parameters $C^{(1)}-C^{(3)}$, $\omega^{(1)}-\omega^{(3)}$, and $\gamma^{(1)}-\gamma^{(3)}$ are determined by fitting the experimental IR line shape. In eqs 33 and 34, the Lorentz factor $1/(\omega_{IR} - \omega_m + i\gamma_m)$ for the IR active modes 2 and 3 is substituted with $g(\omega_{IR})$ in eq 35.

ii. Local Field Correction s. In the isotropic bulk region, the local field correction factor is given by the Lorentz model,[52,53]

$$s_x(\omega) = \frac{n(\omega)^2 + 2}{3} \qquad s_z(\omega) = \frac{n(\omega)^2 + 2}{3n(\omega)^2}$$

$$(36)$$

where $n(\omega)$ is the refractive index at the frequency ω. The dispersion for $n(\omega)$ was considered using the relation given in ref 54.

iii. Experimental Geometry. The geometrical conditions of the SFG measurement were taken from the experiment by Hommel and Allen.[9,55] The visible wavelength is fixed to 800 nm,

while the infrared wavenumber ranges from 2900 cm^{-1} to 3150 cm^{-1}. As depicted in Figure 14, the incident angles for the visible and infrared are $\theta^{\alpha}_{vis} = 58°$ and $\theta^{\alpha}_{IR} = 67°$,[55] and the SFG signal is detected in the reflected direction. The wave vectors in eq 30 are calculated using the relation $|k^{\beta}| = n^{\beta}(\omega)\omega/c$, the Snell's law, and the momentum conservation condition, $k^{\beta}_{SF,x} = k^{\beta}_{vis,x} + k^{\beta}_{IR,x}$.

C. Results and Discussion. Figure 15a shows the bulk contributions, $Im[\chi^{IQB}_{yyz}]$ (red solid line) and $Im[\chi^{B}_{yyz}]$ (red

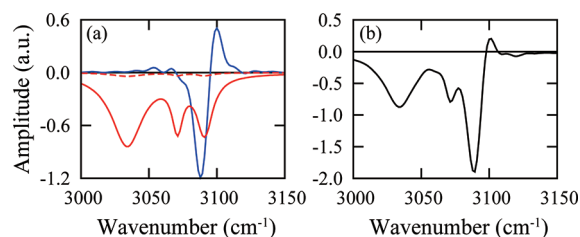**Figure 15.** (a) Surface and bulk contributions to the imaginary part of susceptibility. The blue line denotes the surface contribution $Im[\chi^{MD}_{yyz}]$, the red solid line is $Im[\chi^{IQB}_{yyz}]$, and the red dashed line is $Im[\chi^{B}_{yyz}]$. (b) Total imaginary part including surface and bulk contributions.

dashed line), to the imaginary part of the extended nonlinear susceptibility $\chi^{(2)}_{q\,yyz}$. We see from this figure that the χ^{B} term is negligibly small compared to the χ^{IQB} term. This fact is consistent to previous study elucidating that the χ^{B} term is small for the SSP polarization.[23] We conclude that most of the bulk contribution is attributed to the χ^{IQB} term in the SFG of liquid benzene, which is essentially inseparable from the interface contribution by experimental measurement. Panel a also shows the interface contribution calculated in Section IV, $Im[\chi^{MD}_{yyz}]$ (blue line), in comparison with the bulk contributions. It is noted that the interface contribution corresponds to $\chi^{MD}_{yyz} + \chi^{IQ}_{yyz}$ in eq 26. Comparing the surface and bulk contributions in panel a, we found that the bulk contribution is as large as the interface one. The bulk term $Im[\chi^{IQB}_{yyz} + \chi^{B}_{yyz}]$ is split into three bands with the negative phase, while the surface term $Im[\chi^{ID}_{yyz} + \chi^{IQ}_{yyz}]$ is split into two bands with opposite phases. We note that the mechanism of the splitting is different; the bulk term is split by the Fermi resonance of the IR-active ν_{20} mode, while the surface term is split by forming local modes at the interface. Panel b of Figure 15 displays the imaginary part of the total nonlinear susceptibility $Im[\chi^{(2)}_{q\,yyz}]$ including both the surface and the bulk contributions. The total line shape is qualitatively distinct from that of the surface term or the bulk term.

Figure 16 shows the intensity spectrum of SSP-polarized SFG from the liquid benzene. The line shape of the intensity spectrum

is calculated by eq 25 as $I_{SSP} \propto |\chi^{(2)}_{q,yyz}|^2$. The calculated spectrum in panel a reproduces the experimental spectrum in panel b well.[9]

VI. CONCLUSION

In this study, we elucidated the mechanisms of SFG of liquid benzene from two standpoints: the symmetry breaking at the interface and the bulk contribution. Since a benzene molecule with inversion symmetry has null hyperpolarizability in itself, the SFG signal of benzene must require symmetry breaking at the interface within the dipole approximation. We also evaluated the bulk contribution of quadrupole origin beyond the dipole approximation. We found that both contributions are of comparable significance in the observed SFG signal.

At the interface, the six C−H stretching vibrational modes in quasi-degenerate states should be readily mixed by anisotropic perturbation to form local modes. As a result, the local modes which originate from the IR-active ν_{20} and Raman-active ν_{2} modes are mainly detected in the SSP-polarized SFG spectrum. Regarding the bulk contributions, we found that the χ^{IQB} term is dominant while χ^{B} has minor contributions. The χ^{IQB} term in the SSP-polarized spectrum is attributed to the ν_{20} mode in the bulk liquid and accordingly split by the Fermi resonance. We have to take into account both the surface and the bulk contributions to analyze the line shape of the SFG spectrum of benzene.

The importance of the quadrupole contribution would be surprising in the vibrational SFG spectrum. One could point out two issues to emphasize the quadrupole effect of benzene. First, since the dipole contribution would be prohibited without the anisotropic perturbation, the higher-order quadrupole contribution could become relatively important. Second, the benzene molecule has a considerable quadrupole moment in its equilibrium geometry. In fact, Matsuzaki et al. argue that quadrupolar contribution is predominant in SFG from liquid benzene based on their experimental $Im[\chi^{(2)}]$ spectra obtained by heterodyne-detected SFG spectroscopy.[56,57]

The present SFG analysis of the benzene surface can be straightforwardly applied to other liquids composed of centro-symmetric molecules. It is interesting to evaluate the relative significance of the two mechanisms in the SFG spectra of other systems. Considering these mechanisms in SFG spectra, that is, the symmetry breaking at the interface and the bulk contribution, will be of general significance toward further development of sophisticated and accurate theory of SFG.

■ APPENDIX A. FITTING PROCEDURE OF FORCE CONSTANTS

This appendix presents the fitting procedure of the quadratic force constants $k_{i,j}$ in eq 2, or more specifically eq 3.
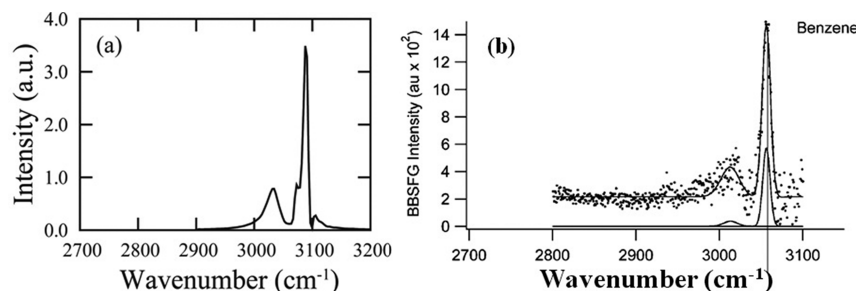

Figure 16. Comparison of (a) calculation and (b) experiment[9] for the SSP-polarized SFG intensity spectrum. Reprinted with permission from ref 9. Copyright 2003, Royal Society of Chemistry.

The intramolecular potential u_{intra} eq 2 derives the following form of Hessian, H_{pq}^{eq},

$$H_{pq}^{eq} = \left(\frac{\partial^2 u_{intra}}{\partial x_p \partial x_q}\right)^{eq} = \sum_{i,j=1}^{30} k_{i,j} \left(\frac{\partial S_i}{\partial x_p}\right)^{eq} \left(\frac{\partial S_j}{\partial x_q}\right)^{eq} \tag{37}$$

where x_p and x_q ($p,q = 1-3N_{atom}$) are the Cartesian coordinates of the atoms of benzene, and the superscript eq indicates the values defined at the equilibrium geometry. The derivative $(\partial S/\partial x)$ is often called the B matrix in the theory of molecular vibration.[41] In this appendix we omit the superscript equation in the following.

The quadratic force constants, $k_{i,j}$, were determined with the help of density functional calculation (DFT) and the experimental vibrational frequencies in the following manner. First the DFT calculation for the harmonic vibrations of benzene was performed at the level of B3LYP/cc-pVTZ, and the calculated Hessian by the DFT is denoted with $H_{pq}(calc)$. Then the mass-weighted Hessian, $K_{pq}(calc)$, is defined by $K_{pq}(calc) = H_{pq}(calc)/(m_p m_q)^{1/2}$, where m_p is the mass of the atom associated to the coordinate x_p. The normal modes and their frequencies are obtained by diagonalizing the mass-weighted Hessian $K(calc)$,

$$P^t K(calc) P = \begin{pmatrix} \omega_1(calc)^2 & & 0 \\ & \ddots & \\ 0 & & \omega_{36}(calc)^2 \end{pmatrix} \tag{38}$$

where $\omega_1(calc)-\omega_{36}(calc)$ are the harmonic frequencies by the DFT calculation, including six zero modes for translation and rotation. Each column of the matrix P represents the displacement vector of normal mode. The displacement vectors for the C–H stretching vibrational modes are called F_1-F_6 in the main text (see Figure 4).

We are aware that the calculated harmonic frequencies $\omega_1(calc)-\omega_{36}(calc)$ somewhat deviate from the experimental frequencies $\omega_1(exp)-\omega_{36}(exp)$,[31] because of limited accuracy of the calculation and anharmonicity. Therefore, we modify the calculated Hessian $K(calc)$ so as to reproduce the experimental frequencies. The modified Hessian $K(mod)$ is given as

$$K(mod) = P \begin{pmatrix} \omega_1(exp)^2 & & 0 \\ & \ddots & \\ 0 & & \omega_{36}(exp)^2 \end{pmatrix} P^t \tag{39}$$

The independent, nonzero components of the quadratic force constants, $k_{i,j}$, are determined by the least-squares fitting that the model Hessian in eq 37 reproduces the modified Hessian $K(mod)$ in eq 39. The optimized results of $k_{i,j}$ are summarized in Table 1. The model Hessian with the optimized force constants reproduces the experimental frequencies very well.

■ AUTHOR INFORMATION

Corresponding Author
*E-mail: morita@m.tohoku.ac.jp.

Notes
The authors declare no competing financial interest.

■ ACKNOWLEDGMENTS

■ REFERENCES

(1) Shen, Y. R. *The principles of nonlinear optics*; Wiley: New York, 1984.
(2) Heinz, T. F. In *Nonlinear Surface Electromagnetic Phenomena*; Ponath, H.-E., Stegeman, G. I., Eds.; Elsevier: Amsterdam, 1991; p 353.
(3) Buck, M.; Himmelhaus, M. *J. Vac. Sci. Technol., A* **2001**, *19*, 2717.
(4) Bain, C. D. *J. Chem. Soc., Faraday Trans.* **1995**, *91*, 1281.
(5) Richmond, G. L. *Chem. Rev.* **2002**, *102*, 2693.
(6) Shen, Y. R.; Ostroverkhov, V. *Chem. Rev.* **2006**, *106*, 1140.
(7) Allen, H. C.; Casillas-Ituarte, N. N.; Sierra-Hernandez, M. R.; Chen, X.; Tang, C. Y. *Phys. Chem. Chem. Phys.* **2009**, *11*, 5538.
(8) Shultz, M. J.; Schnitzer, C.; Simonelli, D.; Baldelli, S. *Int. Rev. Phys. Chem.* **2000**, *19*, 123.
(9) Hommel, E. L.; Allen, H. C. *Analyst* **2003**, *128*, 750.
(10) Ishiyama, T.; Morita, A. *J. Phys. Chem. C* **2007**, *111*, 721.
(11) Ishiyama, T.; Morita, A. *J. Phys. Chem. C* **2007**, *111*, 738.
(12) Ishiyama, T.; Morita, A. *J. Chem. Phys.* **2009**, *131*, 244714.
(13) Ishiyama, T.; Morita, A. *J. Phys. Chem. C* **2011**, *115*, 13704.
(14) Ishiyama, T.; Sokolov, V. V.; Morita, A. *J. Chem. Phys.* **2011**, *134*, 024509.
(15) Ishiyama, T.; Sokolov, V. V.; Morita, A. *J. Chem. Phys.* **2011**, *134*, 024510.
(16) Terhune, R. W.; Maker, P. D.; Savage, C. M. *Phys. Rev. Lett.* **1962**, *8*, 404.
(17) Pershan, P. S. *Phys. Rev.* **1963**, *130*, 919.
(18) Adler, E. *Phys. Rev.* **1964**, *134*, A728.
(19) Bloembergen, N.; Chang, R. K.; Jha, S. S.; Lee, C. H. *Phys. Rev.* **1968**, *174*, 813.
(20) Yamaguchi, S.; Shiratori, K.; Morita, A.; Tahara, T. *J. Chem. Phys.* **2011**, *134*, 184705.
(21) Held, H.; Lvovsky, A. I.; Wei, X.; Shen, Y. R. *Phys. Rev. B* **2002**, *66*, 205110.
(22) Byrnes, S. J.; Geissler, P. L.; Shen, Y. R. *Chem. Phys. Lett.* **2011**, *516*, 115.
(23) Shiratori, K.; Morita, A. submitted for publication, 2012.
(24) Morita, A.; Hynes, J. T. *Chem. Phys.* **2000**, *258*, 371.
(25) Morita, A.; Hynes, J. T. *J. Phys. Chem. B* **2002**, *106*, 673.
(26) Morita, A.; Ishiyama, T. *Phys. Chem. Chem. Phys.* **2008**, *10*, 5801.
(27) Morita, A.; Kato, S. *J. Am. Chem. Soc.* **1997**, *119*, 4021.
(28) Morita, A.; Kato, S. *J. Phys. Chem. A* **2002**, *106*, 3909.
(29) Ishida, T.; Morita, A. *J. Chem. Phys.* **2006**, *125*, 074112.
(30) Morita, A. *Chem. Phys. Lett.* **2004**, *398*, 361.
(31) Oki, M. *Kagaku Binran (Japanese)*, 4th ed.; Maruzen: Tokyo, 1993.
(32) Guest, M. F.; Bush, I. J.; Dam, H. J. J. v.; Sherwood, P.; Thomas, J. M. H.; van Lenthe, J. H.; Havenith, R. W. A.; Kendrick, J. *Mol. Phys.* **2005**, *103*, 719.
(33) Janowski, T.; Pulay, P. *Chem. Phys. Lett.* **2007**, *447*, 27.
(34) Fincham, D. *Mol. Simul.* **1994**, *13*, 1.
(35) Misawa, M.; Fukunaga, T. *J. Chem. Phys.* **1990**, *93*, 3495.
(36) Narten, A. H. *J. Chem. Phys.* **1968**, *48*, 1630.
(37) Rathbun, R. E.; Babb, A. L. *J. Phys. Chem.* **1961**, *65*, 1072.
(38) Majer, V.; Svoboda, V. *Enthalpies of Vaporization of Organic Compounds: a critical review and data compilation*; Blackwell Science Publications: Oxford, 1985.
(39) Varsanyi, G. *Assignment for Vibrational Spectra of Seven Hundred Benzene Derivatives*; Wiley: New York, 1971; Vol. *1*.
(40) Varsanyi, G.; Szoke, S. *Vibrational spectra of benzene derivatives*; Academic Press: New York, 1969.

(41) Wilson, E. B.; Decius, J. C.; Cross, P. C. *Molecular Vibrations*; Dover: New York, 1955.

(42) Townsend, R. M.; Gryko, J.; Rice, S. A. *J. Chem. Phys.* **1985**, *82*, 4391.

(43) Townsend, R. M.; Rice, S. A. *J. Chem. Phys.* **1991**, *94*, 2207.

(44) Matsumoto, M.; Kataoka, Y. *J. Chem. Phys.* **1988**, *88*, 3233.

(45) Taylor, R. S.; Dang, L. X.; Garrett, B. C. *J. Phys. Chem.* **1996**, *100*, 11720.

(46) Nihonyanagi, S.; Yamaguchi, S.; Tahara, T. *J. Chem. Phys.* **2009**, *130*, 204704.

(47) Chen, X.; Hua, W.; Huang, Z.; Allen, H. C. *J. Am. Chem. Soc.* **2010**, *132*, 11336.

(48) Stiopkin, I. V.; Weeraman, C.; Pieniazek, P. A.; Shalhout, F. Y.; Skinner, J. L.; Benderskii, A. V. *Nature* **2011**, *474*, 192.

(49) Shiratori, K.; Morita, A. *J. Chem. Phys.* **2011**, *134*, 230705.

(50) Frisch, M. J.; Trucks, G. W.; Schlegel, H. B.; Scuseria, G. E.; Rob, M. A.; Cheeseman, J. R.; Montgomery, J. A., Jr.; Vreven, T.; Kudin, K. N.; Burant, J. C., et al. *Gaussian 03*; Gaussian, Inc.: Wallingford, CT, 2003.

(51) Cances, E.; Mennucci, B.; Tomasi, J. *J. Chem. Phys.* **1997**, *107*, 3032.

(52) Lorentz, H. A. *The Theory of Electrons*; Dover: New York, 1952.

(53) Bottcher, C. J. F. *Theory of Electronic Polarization*, 2nd ed.; Elsevier: Amsterdam, 1978.

(54) Samoc, A. *J. Appl. Phys.* **2003**, *94*, 6167.

(55) Hommel, E. L.; Ma, G.; Allen, H. C. *Anal. Sci.* **2001**, *17*, 1325.

(56) Matsuzaki, K.; Nihonyanagi, S.; Yamaguchi, S.; Nagata, T.; Tahara, T. 1D07, Annual Meeting of Japan Society for Molecular Science, Sapporo, Japan, 2011.

(57) Matsuzaki, K.; Nihonyanagi, S.; Yamaguchi, S.; Nagata, T.; Tahara, T. to be submitted, **2012**.

13182

dx.doi.org/10.1021/jp302684q | *J. Phys. Chem. C* 2012, 116, 13169−13182